Seawater pressure induced by seismic ground motions and tsunamis

Tatsuo Ohmachi[1], Hiroyuki Matsumoto[1], and Hiroshi Tsukiyama[2]

[1]*Department of Built Environment, Tokyo Institute of Technology, Midori-ku, Yokohama, Japan*
[2]*Tsukiyama Research, Inc., Funabashi, Chiba, Japan*

Abstract. Some real-time tsunami monitoring systems observe seawater pressure at the seabed to evaluate the sea surface disturbance. However, the water pressure at the seabed is usually contaminated by several factors to the extent that the evaluation is hardly possible. Among others, earthquake ground motion causes a pressure vibration of large amplitude. In the present study, numerical simulation of tsunamis is conducted taking into account dynamic seabed displacement due to seismic faulting. From the results, the relation between seawater pressure at the seabed and wave height at the sea surface is obtained, and a simple procedure is presented to evaluate the tsunami component from the seawater pressure following an earthquake. The procedure is successfully applied to the actual seawater pressure recorded in a small earthquake off Sanriku, Japan.

1. Introduction

To predict tsunami hazards, real-time monitoring of tsunamis is being conducted in the deep ocean around potentially tsunami-hazardous areas of the world, especially the Pacific Rim (e.g., González *et al.*, 1998). Some of the monitoring systems observe seawater pressure at the seabed, from which wave height of the sea surface is evaluated. However, the evaluation of the wave height from the seawater pressure is not easy, because the seawater pressure indicates frequency-dependent characteristics. The present study aims to obtain relations between the seawater pressure, the water wave height, and ground motions.

Changing widely fault parameters and water depth, we have conducted a numerical simulation in 2 dimensions, and derived a simple procedure to evaluate the tsunami component from the seawater pressure. Using the procedure, a small tsunami component has been detected from the actually observed records of the seawater pressure induced by a small oceanic earthquake. We have also carried out a numerical simulation of this small tsunami and compared it with the observation.

2. Analytical Procedure

In the present tsunami simulation technique, weak coupling is assumed between the sea bed and the seawater. That is, the motion of the seawater
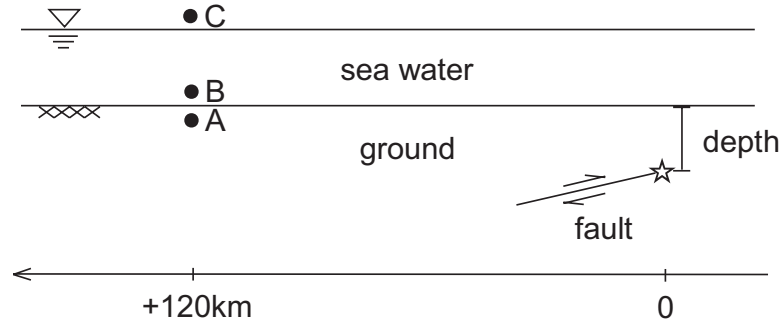

Figure 1: Analytical model.

is influenced by that of the seabed, but the motion of the seabed is not influenced by that of the seawater. Based on this assumption, seawater disturbance including tsunamis is simulated by providing the fluid domain at the seabed with the velocity of the earthquake motion of the seabed as an input. Consequently, the present analysis consists of a two-step simulation. The first step is to simulate the dynamic seabed displacement resulting from a seismic faulting, and the second is to simulate generation of the seawater disturbance followed by the propagation.

For the first step simulation on the seabed displacement, the boundary element method (BEM) (Kataoka and Ohmachi, 1997) is employed here. The second step simulation on the seawater disturbance is conducted with the finite difference method (FDM), which is outlined in the following.

The mass conservation equation and the Navier-Stokes equation shown in (1) and (2) are used as governing equations for the fluid analysis without using the long-wave approximation.

$$\frac{\partial \rho}{\partial t} + \rho \left(\nabla \cdot \boldsymbol{V} \right) = 0 \tag{1}$$

$$\frac{\partial \left(\rho \boldsymbol{V} \right)}{\partial t} + \boldsymbol{V} \cdot \nabla \left(\rho \boldsymbol{V} \right) = \rho \boldsymbol{F} - \nabla p + \mu \nabla^2 \boldsymbol{V} \tag{2}$$

in which ρ, $\boldsymbol{V}$, $\boldsymbol{F}$, p, and μ are density, a velocity vector, a force vector, pressure, and viscosity of the fluid, respectively, and ∇ is a differential operator denoting gradient.

If the water is regarded as a limited compressible fluid, the mass conservation equation can be expressed as

$$\frac{1}{a^2} \frac{\partial p}{\partial t} + \rho \left(\nabla \cdot \boldsymbol{V} \right) = 0 \tag{3}$$

in which acoustic wave velocity is denoted by a. Based on (2) and (3), numerical simulation is carried out by means of the extended SOLA method (e.g., Hirt *et al.*, 1975) in 3-dimensions (3-D).

Table 1: Parameters of fault and ground.

fault width	15 km
depth of hypocenter	10 km
dip angle	13°
dislocation	30 cm
rupture velocity	3.0 km/s
rise time	1.0 s
P-wave velocity	5.9 km/s
S-wave velocity	3.5 km/s
density of the ground	26.5 kN/m^3

3. Relation Between Water Pressure and Wave Height

3.1 Analytical model

A series of numerical simulation is carried out in 2-D. As shown in Fig. 1, a thrust faulting is considered in an elastic half-space. The rupture is propagated from the top to the bottom of the fault at a constant rupture velocity. Parameters of the fault and the ground are shown in Table 1. The fault parameters are selected considering an oceanic earthquake mentioned later. Observation points for seabed ground motion, seawater pressure and wave height are 120 km distant from the epicenter denoted by the dots (closed circles) A, B, and C in Fig. 1.

With these conditions, the combination of the rise time τ and the water depth D is changed as shown by circles in Table 2.

3.2 Analytical results

Results of the simulation with $\tau = 1$ s and $D = 900$ m are shown in Figs. 2, 3, and 4, in which the time 0 corresponds to the start of the fault rupturing. The seawater pressures at the seabed shown in Figs. 4a and b are the same, but the scale of their vertical axes is different.

As shown in Fig. 3, two types of seawater waves are generated. One is the wave induced by earthquake ground motion of the seabed shown in Fig. 2, and the other is the tsunami caused by static (residual) displacement of the seabed in the near-fault area. In Fig. 4b, two distinct seawater pressure vibrations are seen in accordance with the two types of seawater waves. The first vibration is propagated at 3 km/s and arrives at the observation point at about 40 s after the fault rupturing. The second vibration is propagated at 100 m/s and arrived at about 700 s after the fault rupturing.

Table 2: Combination rise time τ and water depth D.

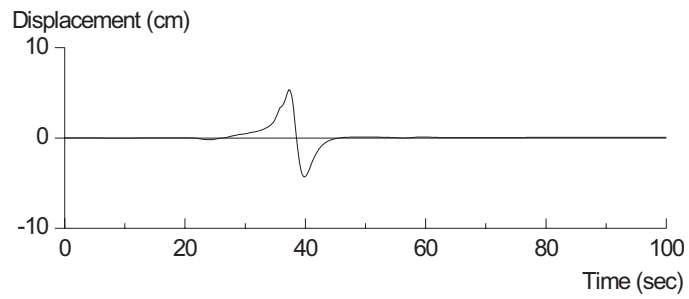| τ	D			
	900 m	1500 m	3000 m	4500 m
1.0 s	◯	◯	◯	◯
5.0 s	◯			
10.0 s	◯			

Figure 2: Ground motion at the seabed (U-D component).
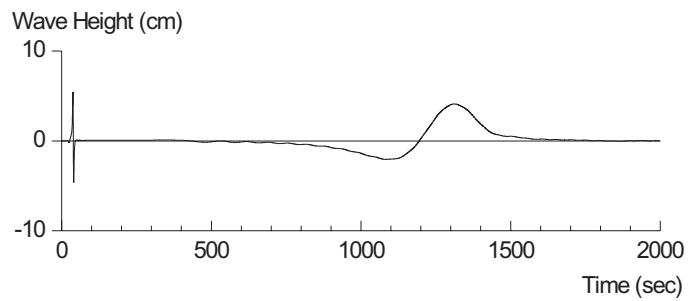

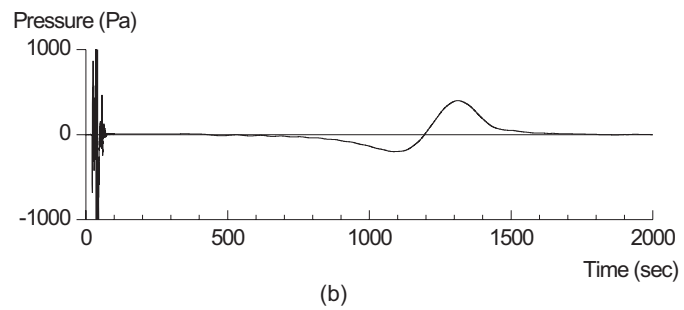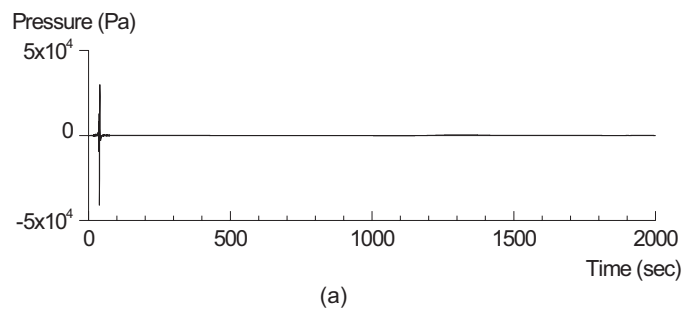**Figure 3**: Wave height at the sea surface.

Figure 4: Seawater pressure at the seabed.

3.3   Effects of rise time

Effects of the rise time on the seawater pressure at the seabed and the wave height at the sea surface are evaluated from the cases where the water depth is kept constant at $D = 900$ m. From the wave height $h(t)$ and the seawater pressure $p(t)$ shown in Figs. 3 and 4, their Fourier amplitude spectra $H(T)$ and $P(T)$ are respectively calculated, and the ratio $H(T)/P(T)$ is plotted against the period on a log-log scale, with a result shown in Fig. 5.

Apparently, in Fig. 5, the spectral ratio shows an increase in proportion with T^2 in a shorter period range, and it is kept constant in a longer period range. The period separating these two ranges is called a corner period T_c hereafter. The constant ratio of $H(T)/P(T)$ above T_c is $1/\rho g$, which corresponds to the static water pressure ρgh. As far as the rise time between 1 s and 10 s is concerned, the corner period T_c is found to be 40 s.

3.4   Effects of the water depth

Effects of the water depth on the seawater pressure at the seabed and the wave height at the sea surface are evaluated from the cases where the rise time is kept constant at $\tau = 1$ s. In Fig. 6, the spectral ratio $H(T)/P(T)$ is plotted in the same way as shown in Fig. 5.

The spectral ratio $H(T)/P(T)$ shown in Fig. 6 shows an increase in proportion with T^2 in a shorter period range, and it is kept constant at $1/\rho g$ in a longer period. As for the corner period T_c, it increases with an increase in the water depth D. That is, for example, $T_c \doteqdot 40$ s for $D = 900$ m, $T_c \doteqdot 60$ s for $D = 1500$ m, $T_c \doteqdot 100$ s for $D = 3000$ m, and $T_c \doteqdot 130$ s for $D = 4500$ m.

From Fig. 7 in which four pairs of the corner period T_c and the water depth D are plotted, the relation between T_c and D is roughly regressed in a simple form as

$$T_c(\text{sec}) \doteqdot 0.035D(\text{m}) \tag{4}$$

4.   A Case Study

4.1   Real-time monitoring system

At the deep ocean off Sanriku, Japan, a real-time monitoring system for earthquakes and tsunamis has been operated by researchers at the University of Tokyo and Tohoku University since 1996 (e.g., Kanazawa, 2000). When an earthquake (M_w 6.1) occurred in the area shown in Fig. 8 on 31 May 1998, a small tsunami was observed by the system for the first time (e.g., Hino *et al.*, 1998). In Fig. 8, the locations of the seismic fault plane and sensors for the monitoring are shown. Two tsunami sensors, TM1 and TM2, are located approximately 69 km from the coast and 1530 m deep in the ocean, and 41 km and 990 m deep, respectively.
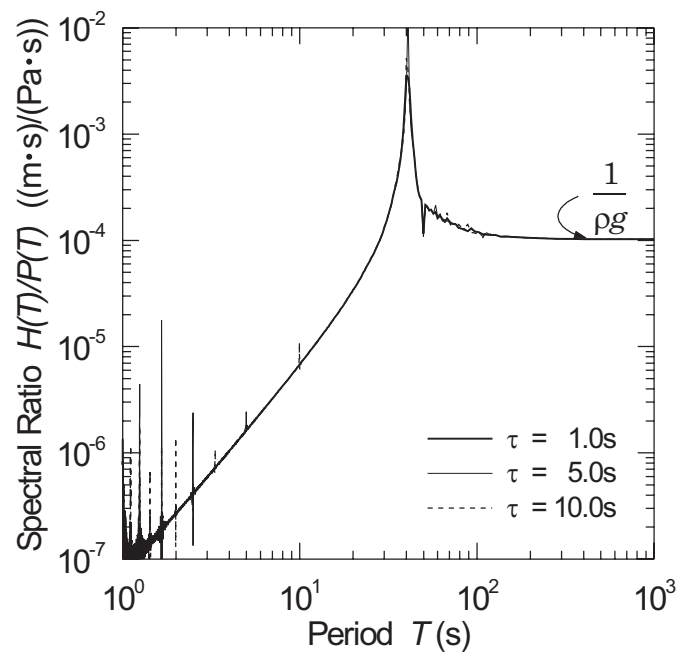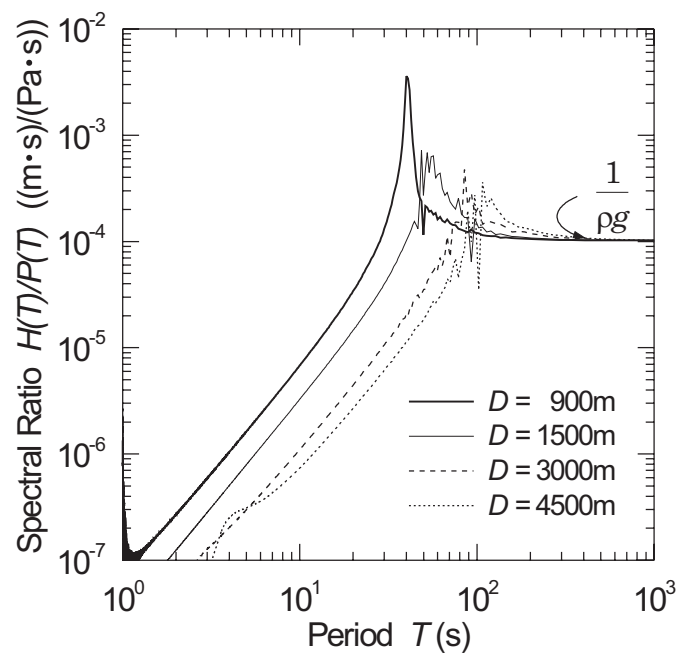
Figure 5: Spectral ratio $H(T)/P(T)$.
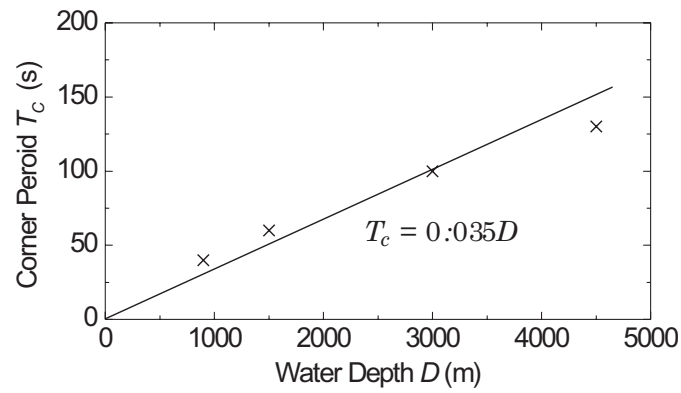

Figure 6: Spectral ratio $H(T)/P(T)$.

Figure 7: Relation between corner period T_c and water depth D.
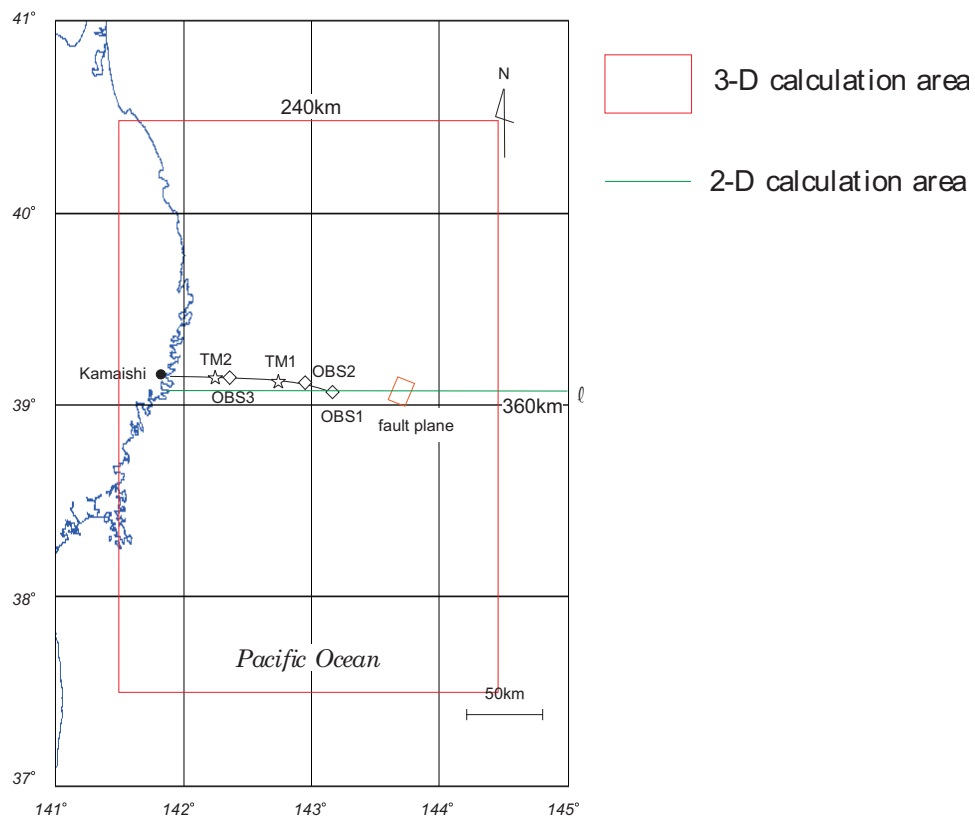

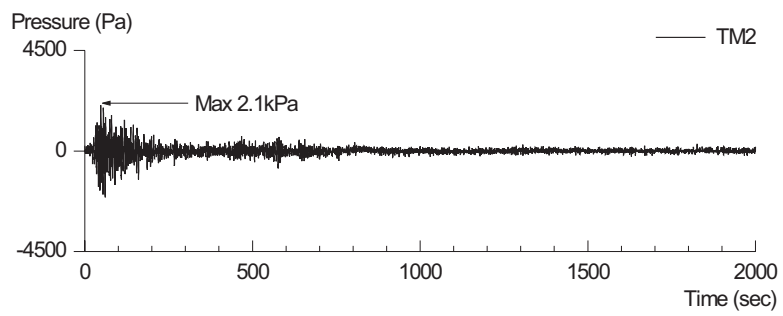**Figure 8**: Location of the fault plane and observed sites.
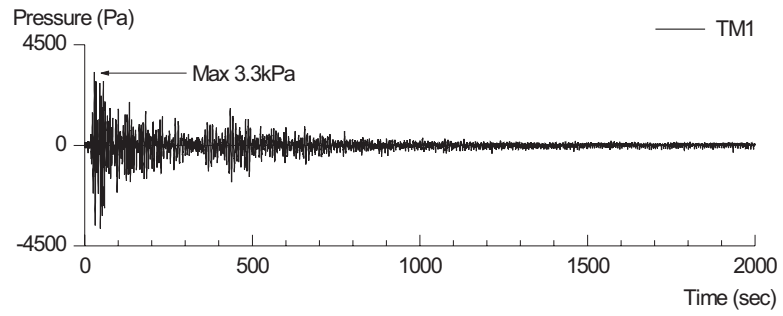
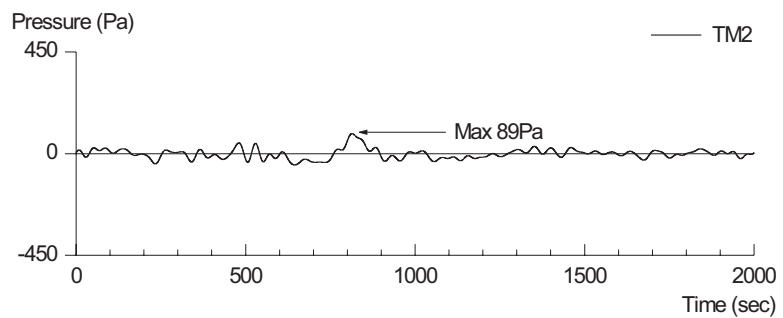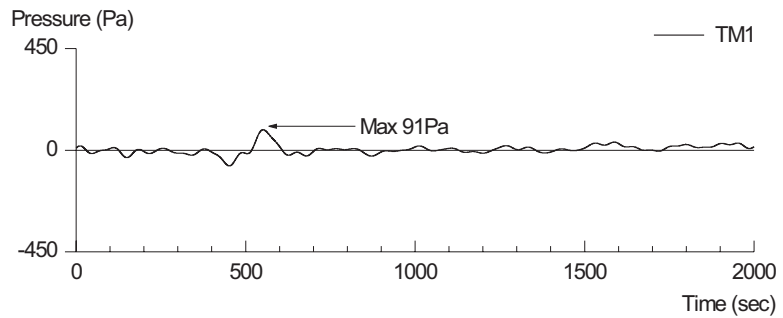**Figure 9**: Seawater pressure records low-pass-filtered at 1 s.

Figure 10: Seawater pressure records low-pass-filtered at corner period T_c.
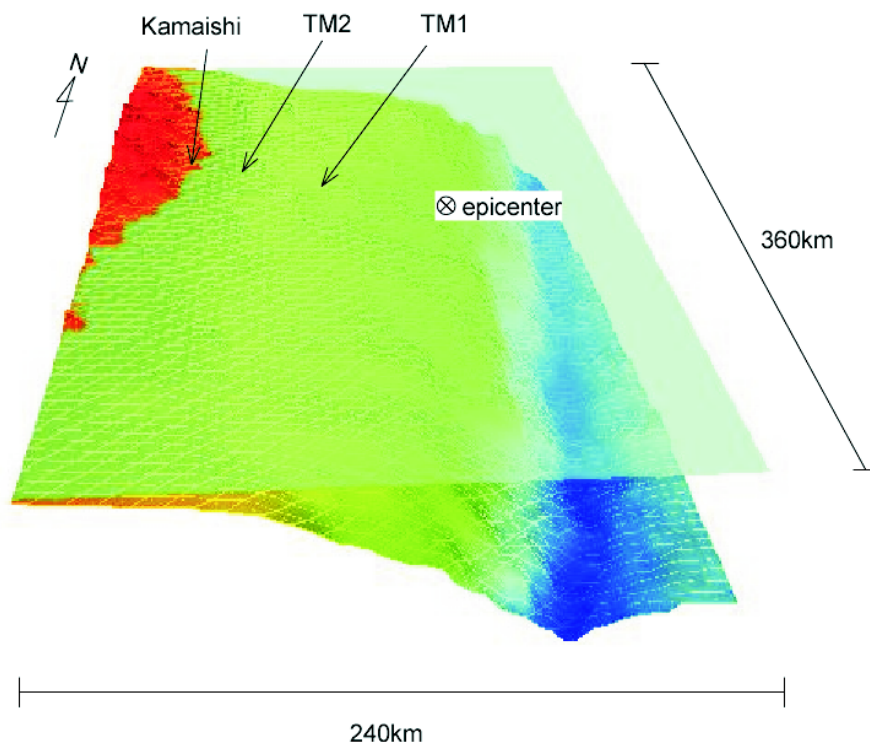
Figure 11: 3-D simulation model.

4.2   Evaluation of tsunami from observed seawater pressure

Since the observed time histories of the seawater pressure are full of high level noises, the noises are removed by low-pass filtering at 1 s. The pressure time histories at TM1 and TM2 thus obtained are shown in Fig. 9, in which time is referred to the main shock that occurred at 3:18:22 JST. In Fig. 9, the maximum seawater pressures 3.3 kPa at TM1 and 2.1 kPa at TM2 are seen at 17 s and 36 s, respectively.

From (4), the corner periods T_c for water depth $D = 1530$ m and $D = 990$ m are $T_c = 54$ s and $T_c = 35$ s, respectively. With these corner periods used for the low-pass filtering, small tsunami components shown in Fig. 10 are obtained from observed seawater pressure records in Fig. 9. The seawater pressures at TM1 and TM2 show a small tsunami arriving at 500 s with the period 200 s and at 800 s with the period 300 s, respectively. In the meantime, the wave height associated with the seawater pressure is 9.1 mm at TM1 and 8.9 mm at TM2.

Consequently, two types of seawater pressure are separated from records, i.e., one is induced by the Rayleigh wave and the other is by the tsunami. It should be noted that the amplitude of the former pressure is much larger than that of the latter, as shown in Figs. 9 and 10.
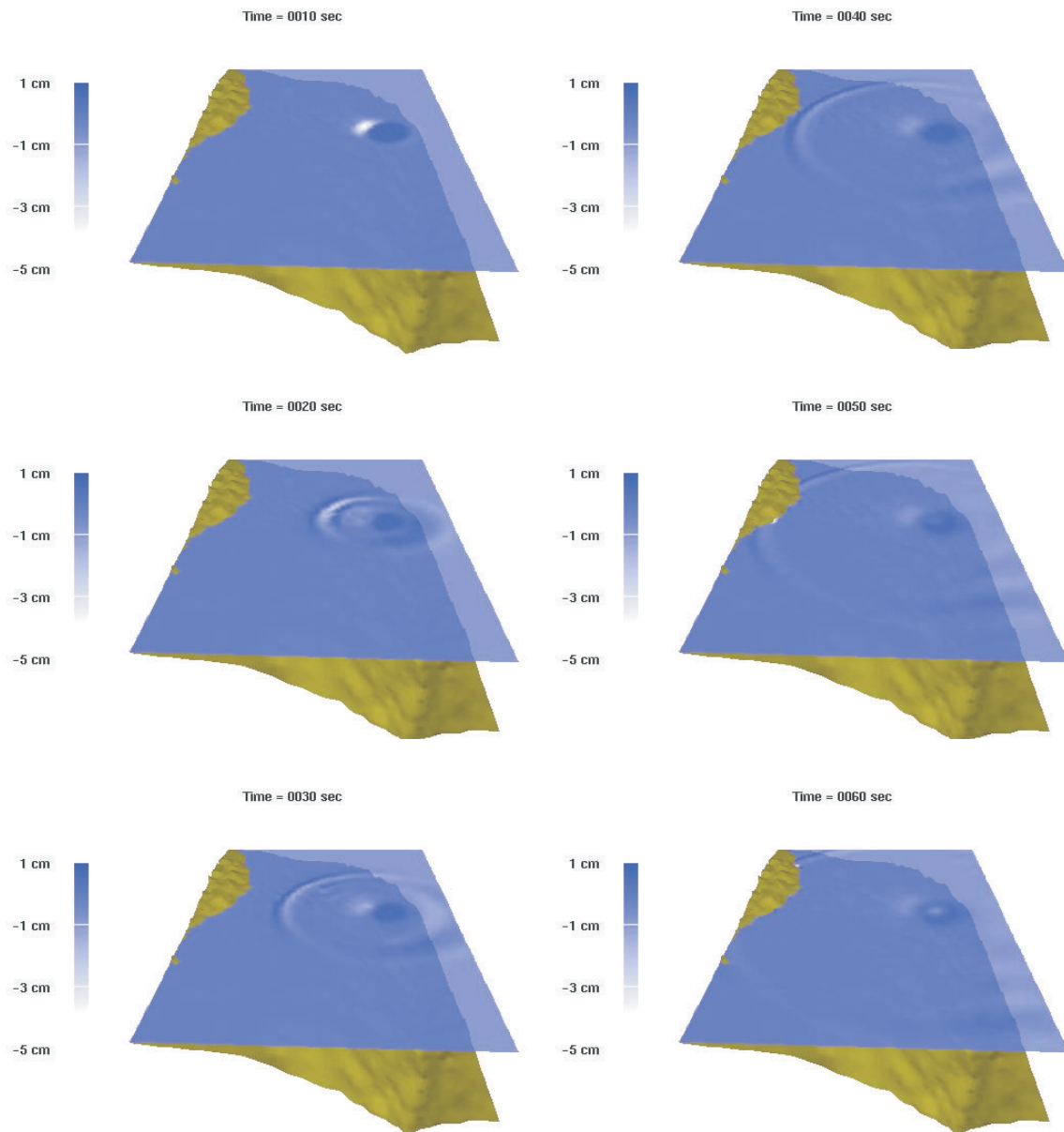
Figure 12: Tsunami generation.

Table 3: Fault parameters.

fault length	15 km
fault width	15 km
depth of hypocenter	10 km
strike	204°
dip angle	13°
rake	95°
dislocation	30 cm
rupture velocity	3.0 km/s
rise time	1.0 s

4.3 Tsunami simulation

The small tsunami mentioned above is simulated here in 3-D. The dotted square in Fig. 8 shows the simulated area which covers 360 km × 240 km in NS and EW directions, respectively. Figure 11 shows an analytical model. The hypocenter of the earthquake is located at 152 km off the coast, and 10 km deep under the seabed. The grid size of BEM used for the seabed motion simulation is 5 km, and the shortest period for the simulation is 2 s. For the simulation of the seawater domain, the grid size is 1 km in the horizontal and vertical directions. After interpolation of the simulated ground motion velocity, the velocity was input to the bottom of the water domain.

The fault rupture is supposed to initiate at the east edge, and to extend westward (e.g., Matsuzawa *et al.*, 1998; Okada *et al.*, 1998). Fault parameters shown in Table 3 are used in the simulation as mentioned in section 3.

Since almost the fault and the observation points are oriented in a straight line, 2-dimensional tsunami simulation along the line ℓ in Fig. 8 is also performed here to compare with the 3-D simulation.

Snapshots in Fig. 12 show sea surface disturbance resulting from the simulation at every 10 s up to 60 s after the fault rupturing. A water wave propagating concentricly is much associated with the Rayleigh wave propagating along the seabed. This water wave passes TM1 and TM2 at about 30 s. The water wave generated near the hypocenter during 40 and 60 s after the fault rupturing is the tsunami caused by the static displacement of the seabed.

Snapshots in Fig. 13 show the tsunami at every 200 s up to 1200 s after the fault rupturing. The arrival time of tsunami at TM1 and TM2 is about 600 s and 800 s, respectively.
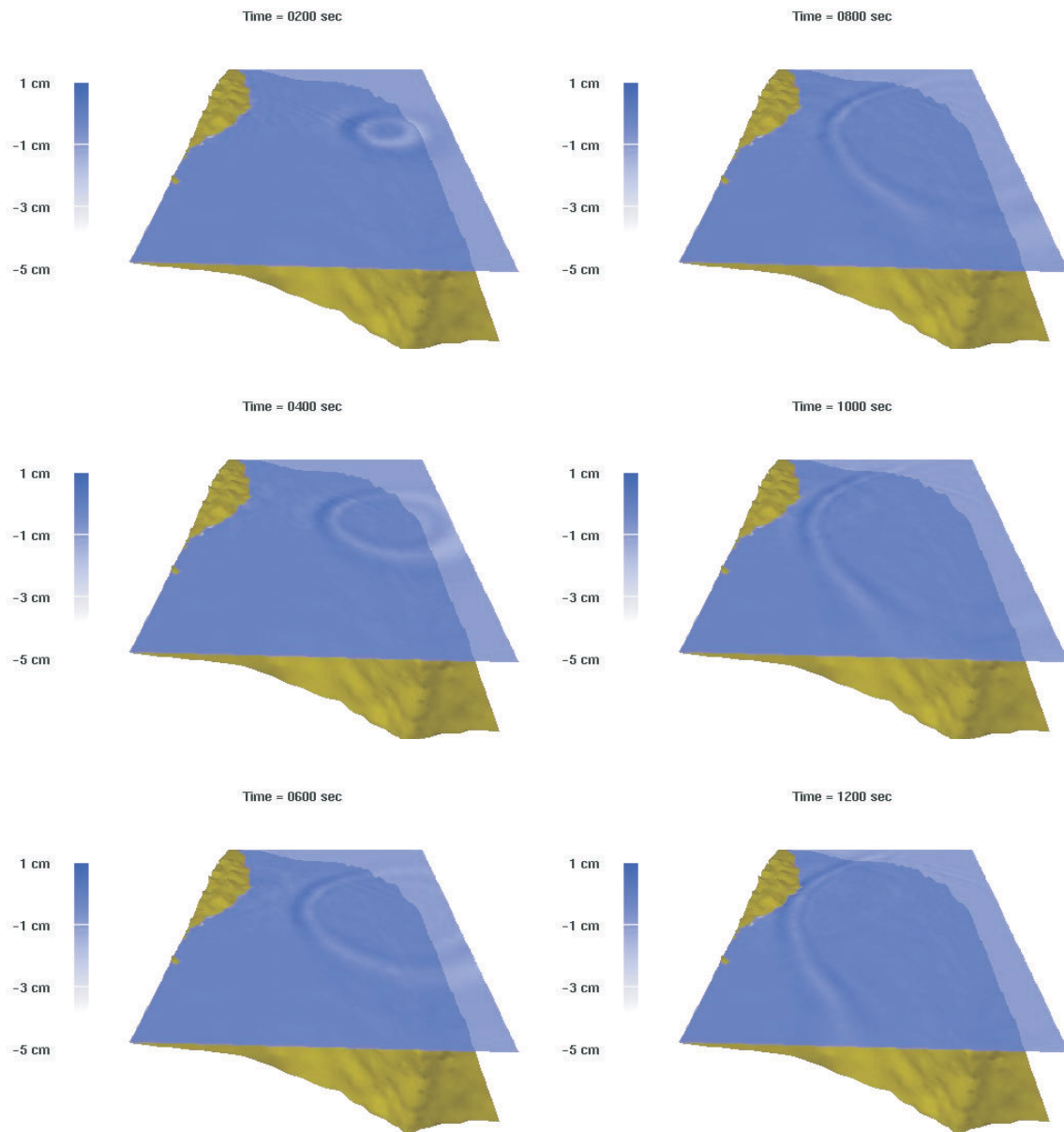
Time = 0200 sec

1 cm

−1 cm

−3 cm

−5 cm

Time = 0800 sec

1 cm

−1 cm

−3 cm

−5 cm

Time = 0400 sec

1 cm

−1 cm

−3 cm

−5 cm

Time = 1000 sec

1 cm

−1 cm

−3 cm

−5 cm

Time = 0600 sec

1 cm

−1 cm

−3 cm

−5 cm

Time = 1200 sec

1 cm

−1 cm

−3 cm

−5 cm
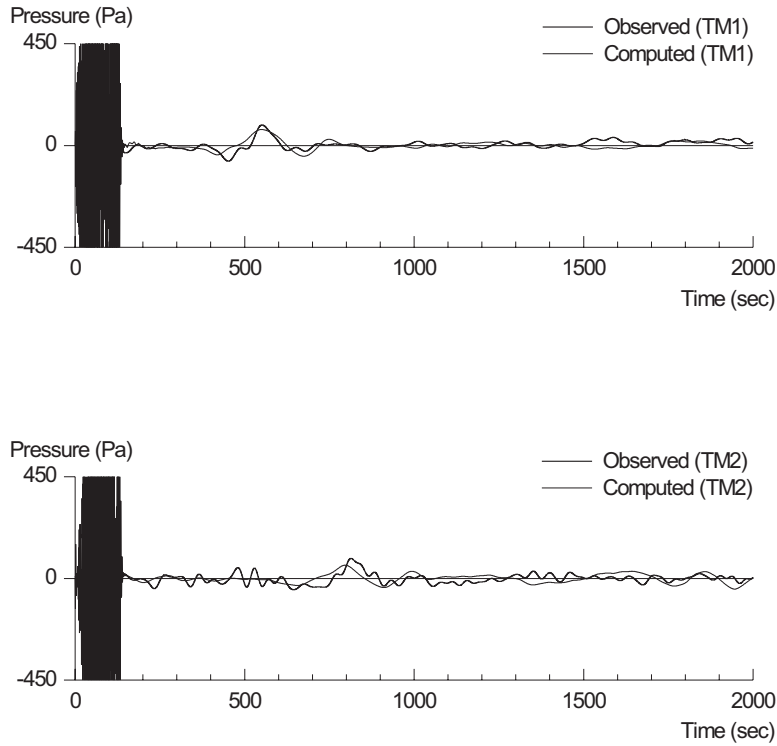
Figure 13: Tsunami propagation.

Figure 14: Seawater pressure simulated in 3-D.

Simulated and observed seawater pressures at TM1 and TM2 are shown in Fig. 14, in which the amplitude of water pressure induced by the Rayleigh wave is overshooting the vertical axis because it is much larger than that of the small tsunami, as shown in Fig. 9. In Fig. 14, the maximum seawater pressures due to the tsunami 70 Pa at TM1 is obtained at 550 s, and 58 Pa at TM2 is obtained at 796 s, respectively. Both the amplitude and the arrival time of the simulated tsunami agree well with that of the observation. Figure 15 shows the 2-D analytical results. The seawater pressure due to the tsunami reaches TM1 and TM2 at 500 s and 800 s, respectively, with the period 250 s. The arrival time of the simulated tsunami agrees well with that of the observation. However, the amplitude of the simulated tsunami is about 5 times as large as that of the observation, suggesting less attenuation in 2-D analysis.

5.   Conclusion

The following conclusions can be drawn from the present study:

1. The relation between seawater pressure p at the seabed and wave height h at the sea surface varies with the period T of the water pressure. In the period range longer than the corner period T_c, the water pressure increases proportionally with an increase in the wave height h only, as expressed $\Delta p = \rho g h$. However, in the period range shorter than T_c,
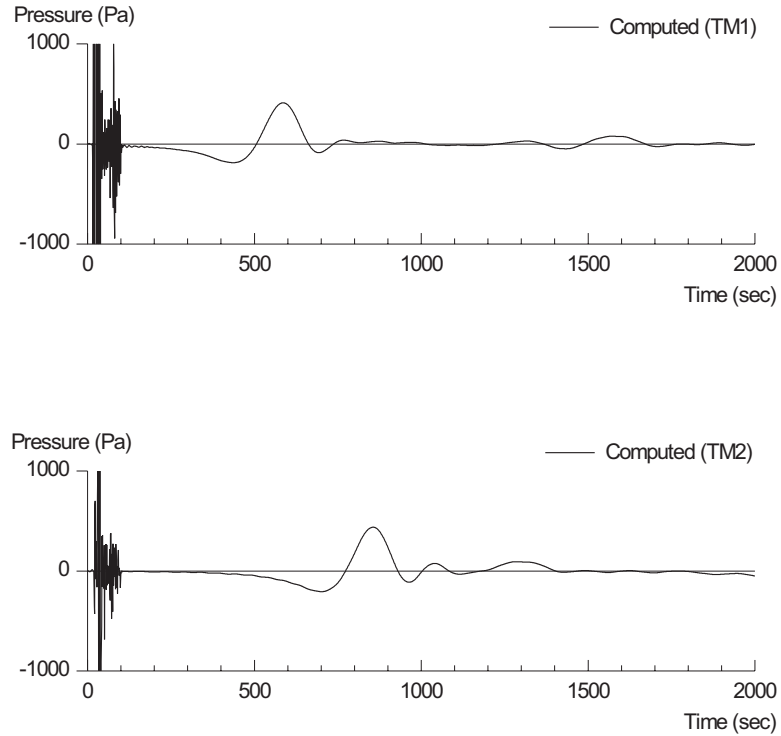
Figure 15: Seawater pressure simulated in 2-D.

the water pressure to wave height ratio $h/\Delta p$ increases in proportion with T^2.

2. The corner period T_c is almost proportional to the water depth D, and roughly expressed as $T_c \doteqdot 0.035D$ where units for T_c and D are s and m, respectively.

3. A simple procedure to evaluate the tsunami component from the time histories of seawater pressure has been successfully applied to the observed pressure records for the small tsunami that occurred on 31 May 1998, off Sanriku, Japan.

4. The 3-D numerical simulation for the small tsunami has demonstrated its validity, and suggested that much care is needed for the use of 2-D simulation because of less attenuation in the wave height.

6.   References

González, F.I., H.M. Milburn, E.N. Bernard, and J.C. Newman (1998): Deep-ocean Assessment and Reporting of Tsunamis (DART): Brief Overview and Status Report. *Proceedings of the International Workshop on Tsunami Disaster Mitigation*, 19–22.

Hino, R., T. Kanazawa, S. Sakai, Y. Tanioka, and K. Suehiro (1998): Tsunamis from an off-Sanriku and the Papua New Guinea earthquakes observed by ocean bottom tsunami measurement. *Progr. Abstr. Seism. Soc. Japan, 2*(P23) (in Japanese).

Hirt, C.W., B.D. Nichols, and N.C. Romero (1975): SOLA–A Numerical Solution Algorithm for Transient Fluid Flows. *Los Alamos Scientific Laboratory report*, LA-5852.

Kanazawa, T. (2000): Measurement at the Seabed–Development of Ocean-bottom Seismometer. *J. Japan Soc. Civil Eng., 85*, January (in Japanese).

Kataoka, S., and T. Ohmachi (1997): 3-D simulation of near-field motion in irregular ground. *J. Structual Mech. Earthquake Eng., 556*(I–38), 139–149 (in Japanese).

Matsuzawa, T., R. Hino, N. Umino, A. Hasegawa, T. Kanazawa, and S. Sakai (1998): On M6.3 earthquake off Sanriku on May 31, 1998, (1) Aftershock Hypocenter Distribution. *Progr. Abstr. Seismol. Soc. Japan, 2*(P21) (in Japanese).

Okada, T., T. Matsuzawa, R. Hino, A. Hasegawa, and T. Kanazawa (1998): On M 6.3 earthquake off Sanriku on May 31, 1998, (2) Source Process. *Progr. Abstr. Seism. Soc. Japan, 2*(P22) (in Japanese).